Cryo-EM Structure of the Mnx Protein Complex Reveals a Tunnel Framework for the Mechanism of Manganese Biomineralization

Irina V. Novikova,^{1,§} Alexandra V. Soldatova,^{2,§} Trevor H. Moser,¹ Stephanie Thibert,¹ Christine A. Romano,³, Mowei Zhou,^{1,+} Bradley M. Tebo,^{2,3} James E. Evans,^{*,1} and Thomas G. Spiro^{*,2}

- 1. Environmental Molecular Sciences Laboratory, Pacific Northwest National Laboratory, 3335 Innovation Blvd, Richland, WA 99354, United States
- 2. Department of Chemistry, University of Washington, Box 351700, Seattle, Washington 98195, United States
- 3. Division of Environmental and Biomolecular Systems, Institute of Environmental Health, Oregon Health & Science University, Portland, Oregon 97239, United States

ABSTRACT

The global manganese cycle relies on microbes to oxidize soluble Mn(II) to insoluble Mn(IV) oxides. Some microbes require peroxide or superoxide as oxidants, but others can use O₂ directly, via multicopper oxidase enzymes. One of these, MnxG from *Bacillus* sp. strain PL-12, was isolated in tight association with small accessory proteins, MnxE and MnxF. The protein complex, called Mnx, has eluded crystallization efforts, but we now report the 3D structure of a point mutant using cryo-EM single particle analysis, cross-linking mass spectrometry, and AlphaFold Multimer prediction. The β-sheet-rich complex features MnxG enzyme, capped by a heterohexameric ring of alternating MnxE and MnxF subunits, and a tunnel that runs through MnxG and its MnxE₃F₃ cap. The tunnel dimensions and charges can accommodate the mechanistically inferred binuclear manganese intermediates. Comparison with the Fe(II)-oxidizing multicopper oxidase, ceruloplasmin, identifies likely coordinating groups for the Mn(II) substrate, at the entrance to the tunnel. Thus, the 3D structure provides a rationale for the established manganese oxidase mechanism, and a platform for further experiments to elucidate mechanistic details of manganese biomineralization.

INTRODUCTION

Manganese is one of the most important redox-active metals in the Earth's biosphere, where it cycles between the +II, +III, and +IV oxidation states. In its reduced soluble state, it is used for a variety of biological functions, including oxygenic photosynthesis, and as intracellular antioxidant and enzymatic cofactor. Its oxidized forms are largely found as insoluble Mn(III,IV) oxides, which may be used as electron acceptors for anaerobic respiration,^{2–4} or could be coupled to other biogeochemical processes, such as the cycling of carbon, nitrogen, and other trace elements and radionuclides.^{5–7} Mn(II) oxidation and biomineralization by fungi and bacteria is the main route of manganese oxide deposition on Earth and a key driver of the global Mn cycle. ^{6,8,9} Fungi employ Mn(II) oxidation in the breakdown of recalcitrant natural organic matter thereby accessing organic carbon for growth. 10 Mn-oxidizing bacteria may derive a variety of other benefits, including energy generation for chemoautotrophic growth, for breakdown and utilization of organic matter, as a protective mechanism against environmental challenges, or for storage of an electron acceptor. 8,11,12 Intriguingly, the enzyme responsible for Mn(II) oxidation in a large number of phylogenetically diverse groups of bacteria was found to belong to the multicopper oxidase (MCO) family. 13-19 Multicopper oxidases (MCOs) are well-studied and widespread in nature as enzymes that catalyze one-electron oxidation of substrates as diverse as Fe(II) and lignin.^{20,21} They accomplish that by using 4 copper atoms that typically couple the one-electron oxidation of substrates to the sequential reduction of O₂ to H₂O. The conversion of Mn(II) to MnO₂ by bacterial MCOs represents a marked departure from this pattern, which uniquely produces a biomineral. Moreover, the conversion of Mn(II) to MnO₂ involves a twoelectron metal oxidation, and extracting an electron from either Mn(II) or Mn(III) is energetically difficult.

Investigation of the mechanism by which bacterial Mn-oxidizing MCOs function had been hindered by the difficulty of their purification, until the Tebo lab succeeded in producing recombinant Mn oxidase in *E. coli*.²² They did this by expressing four contiguous genes contained in a polycistronic operon, mnxDEFG, from marine *Bacillus* sp. strain PL-12. This operon is conserved in three different Mn(II)-oxidizing *Bacillus* species, including the most studied strain SG-1, where manganese-oxidizing MCO was first identified using mutational analysis.^{13,23,24} The MCO protein from PL-12, MnxG (138 kDa), was isolated in tight association with three copies each of two small (12 kDa) accessory proteins MnxE and MnxF,²⁵ which were

required for optimal activity—a feature unprecedented for other known MCOs. For simplicity, we refer to this complex as Mnx. Mnx also appears to be unique to the Mn(II)-oxidizing *Bacillus* species as there are no known homologues of MnxE or MnxF in other organisms. Systematic physical measurements with the purified manganese-oxidizing Mnx complex have offered a mechanism, in which energetic barriers for Mn oxidation are circumvented through formation of hydroxide-bridged binuclear Mn complexes in all three oxidation states: II, III, and IV, on the path to MnO2 production.^{26,27} However, the mechanism remained provisional in the absence of structural elaboration.

Mnx (211 kDa) is too large for NMR structure determination, and an x-ray crystal structure has eluded us because the protein complex is reluctant to crystallize. A global view of enzyme assembly was offered by native mass spectrometry, which found that the three copies each of MnxE and MnxF most likely assemble as an alternating hexamer ring on the larger MnxG,²⁸ whose structure could be obtained based on its closest homolog, human ceruloplasmin, the Fe-oxidizing MCO. No homologues of MnxE and MnxF are available.

To obtain atomic level details of the entire Mnx complex 3D structure, we turned to single particle cryo-electron microscopy (cryo-EM). Initial attempts produced only low-resolution models due to preferential orientation and clustering of the particles in the vitreous ice. We suspect that there was also partial unfolding of the protein at the air-water interface. Through meticulous screening and utilizing optimized freezing conditions, we succeeded at obtaining the first 3.4 Å resolution structure of a single-point mutant form of Mnx (H340A). We computed an initial search model with AlphaFold^{2,29,30} and used the experimental cryo-EM volume to refine this model further. The resulting fitted 3D structure also matched all experimental constraints from crosslinking and native MS.

Strikingly, the structure supports the previously proposed mechanism of biomineralization which involves binuclear Mn complexes in successively higher oxidation states. These intermediates could be accommodated by a tunnel running straight through the complex, with negatively charged and coordinating ligands lining the tunnel walls.

EXPERIMENTAL METHODS

Cryo-EM sample preparation, imaging, and single particle analysis. Mnx H340A mutant gene synthesis, protein synthesis and purification were described previously.³¹ Sample vitrification was performed using a Leica EM GP instrument, preset at 90% humidity and 10 °C. For TEM substrates, Quantifoil R 1.2/1.3 grids with 300 mesh Cu were glow-discharged at 15 mA for 60 s using PELCO easiGlow. Immediately prior plunge-freezing, a solution of the Mnx-H340A complex (6 µl, 5.6 mg/ml in 20 mM HEPES with 150 mM NaCl buffer at pH 7.8) was combined with CHAPSO (1.5 µl, 40 mM) using gentle pipetting. Subsequently, 3 µl of the mixture was applied to the grid, which was then blotted for 4 s before being plunged into liquid ethane. The grid was further clipped and transferred to the autoloader at liquid nitrogen temperature conditions. Cryo-EM data were collected on a 300 keV Titan Krios G3i microscope (ThermoFisher) equipped with a Gatan K3 direct electron detector. The collected dataset of 4,086 image stacks were acquired at the following conditions: 130,000 magnification, 1.34 s exposure, 50 frames per image at a total dose of 50 e/Å² and at super-resolution pixel size of 0.34 Å. The pixel size was previously calibrated against an apoferritin dataset, yielding a 0.68 Å pixel size for non-super-resolution mode at this magnification. Data processing was performed in cryoSPARC v4.4.1 software. 32,33 All images were initially pre-processed using cryoSPARC's patch motion and patch contrast transfer function (CTF) routines and binned by the factor of 2. A blob particle picking method yielded an initial pool of 858,533 picks extracted at 330-pixel box size. This initial particle library was further triaged via three rounds of 2D classification to a final set of 98,663 particles and then subjected to ab-initio reconstruction. The generated ab-initio volume was employed as a 3D reference for non-uniform refinement, resulting in a 3.37Å resolution structure presented in this study (Figure S1). Additional efforts involved conducting refinements through various methods including homogenous, heterogenous and local approaches. However, the non-uniform algorithm achieved the highest resolution. Model Building. An initial atomic model of the Mnx complex was computed with AlphaFold2 Multimer^{29,30} on an in-house server equipped with Nvidia V100 GPUs. A ranked 0.pdb structure with the highest confidence values was then docked to the cryo-EM density in ChimeraX.^{34,35} Several rounds of real space refinement were carried out in PHENIX (Phenix.RealspaceRefine).³⁶ All models and cryo-EM density images were visualized and prepared in ChimeraX.

Chemical crosslinking. Crosslinking was performed by incubating 30 µg of mutant Mnx H340A sample with 5 mM BS3 (bis(sulfosuccinimidyl)suberate) in 50 mM HEPES, pH 7.5, with 150 mM NaCl and 0.005% Tween-20 for 1 h shaking at room temperature in a Thermomixer at 850 rpm. The reaction was quenched by adding 1 M Tris, pH 7.5, to a final concentration of 100 mM and incubating for 10 min at room temperature. Samples were denatured by adding 20% (w/v) SDS in 50 mM Tris, pH 7.5, and solid urea to make final concentrations in the samples 5% (w/v) and 8 M, respectively, and samples were vortexed until the urea was fully dissolved. Samples were then reduced with 5 mM dithiothreitol (DTT) and incubated at 37 °C for 45 min and alkylated with 10 mM iodoacetamide and incubated at room temperature for 45 min in the dark. The reaction was quenched by adding 10 mM DTT and incubating for 10 min at room temperature. All above incubation steps were performed shaking at 850 rpm. Samples were then acidified by adding aqueous phosphoric acid to a final concentration of 2.5% (v/v), diluted with 165 μL of 90% (v/v) methanol in 100 mM Tris, pH 7.5, and loaded onto S-trap micro columns, and protein digestion was performed following the provided protocol (ProtiFi, LLC). Protein digestion was performed at a 1:50 (w/w) ratio of protease: Mnx protein first with Lys-C for 4 h, followed by trypsin overnight, where each step had the protease diluted in a 20 µL final volume in 50 mM Tris, pH 7.5. Sequential elution steps using 40 µL of 50 mM Tris, pH 7.5, 0.2% formic acid in dIH₂O, and 50% acetonitrile in dIH₂O were performed and samples were dried and resuspended in 97/3 dIH₂O/acetonitrile in 0.1% formic acid. Samples were prepared at 0.2 mg/mL in 97/3 dIH₂O/acetonitrile in 0.1% formic acid for LC-MS/MS analysis. Samples were injected onto a Thermo Dionex Ultimate 3000 RSLCnano system with a 4 min loading time at 7 μL/min onto a C2 trapping column using 0.1% formic acid in H₂O (buffer A). Peptides were separated online at a 0.2 µL/min flow rate with a 2 h gradient on an in-house packed column (75 μm i.d., 30 cm long) using 1.7 μm² C18 beads (Waters BEH) starting at 99/1 buffer A/0.1% formic acid in acetonitrile (buffer B) for 2.6 min, then ramping to 8% buffer B for 10 min, 25% buffer B for 95 min, 35% for 10 min, followed by washing the column by raising to 75% buffer B in 5 min, 95% in 3 min and holding for 6 min, reducing to 50% buffer B in 1 min and holding for an additional 1.4 min, and washing again by raising to 95% buffer B for an additional 6 min before returning to 1% buffer B for the remainder of the run. Samples were analyzed using a Thermo Scientific Q Exactive HF-X Hybrid Quadrupole-Orbitrap mass spectrometer with electrospray set to 2,200 V and 325 °C in the ion transfer tube. MS1 scans were acquired

between 300 to 1800 m/z, with a maximum injection time of 10 ms, 3,000,000 AGC target. MS2 was completed using an isolation window of 0.7 m/z and stepped HCD of 20, 30, 40% collision energy, scan range between 200 to 2000 m/z and 30 K resolution. Unassigned, 1, 2, and >8 charge states were excluded and dynamic exclusion was set to 30 s. Raw data were converted to mzML format using ProteoWizard msConvert,³⁷ and analyzed using Merox 2.038 using a semi-unspecific digest, precursor and fragment ion precision set to 10 ppm, and 1% FDR cut-off. Sample data were also analyzed using pLink v2.3.11,³⁹ with all reported crosslink hits manually con-firmed, and those found in the negative controls excluded from the results summary. Identified crosslinks were mapped onto the refined atomic structure using ChimeraX^{34,35} to measure distances between crosslinked residue Cα atoms.

Native mass spectrometry. Purified wild type and Mnx H340A mutant were buffer exchanged twice in 100 mM ammonium acetate using Zeba Spin Desalting Columns, 7K MWCO, diluted to 0.25 mg/mL with a final concentration of 20 mM ammonium acetate, and loaded onto an inhouse pulled glass capillary. A platinum wire was inserted at ground potential and the sample was sprayed using 0.65–0.8 kV capillary voltage onto a Waters Synapt G2-Si in ion-mobility mode with a modified surface induced dissociation device as described previously. Mass spectra were acquired between 500 and 12, 000 m/z with 50 V sampling cone, 30 °C source temperature, 250 °C desolvation temperature, quadrupole manual setting to 6, 000 m/z, and trap gas set to 5 mL/min. IMS wave velocity was set to 450 m/s and IMS wave height set to 23 V. For SID, trap CID was set to 110 V, 100 V collector and 55 V stopper. Spectra were summed over 2–10 minutes, smoothed using +/– 20 windows and 10 smooths using Waters MassLynx. For IM drift time analysis, data were analyzed using Waters DriftScope software.

RESULTS

1. Cryo-EM Data Acquisition Strategies on Mnx H340A Complex Yielded a 3.37Å Map.

We found it extremely challenging to collect cryo-EM data suitable for high quality reconstruction of the Mnx multiprotein complex. Multiple attempts to collect data on the wild type Mnx failed to yield a structure with better than 5Å resolution (data not shown) without evidence of significant overfitting. The main limitation was imposed by Mnx's preferential topview orientation in the thin layer of ice with very close packing, limiting the number of available

projections for 3D reconstruction. We were not able to overcome this problem using various buffer compositions and protein concentrations or collecting tilted data sets. At lower protein concentrations, the particles aggregated or were very dispersed in thicker ice that limited contrast and resolution. There was a suspicion that the protein experienced a partial unfolding at the airwater interface, but it was not obvious from 2D classes of collected datasets as those were always reaching high resolution of 3Å. Despite screening numerous detergents, a dataset obtained from a sample of a point-mutant of Mnx (Mnx H340A) mixed with CHAPSO show no such issues in the reconstructions (Figure S1-S3 and Table S1). The particle pool, just under 100K particles, produced a clearly defined volume without any signs of orientation bias, achieving high cFAR (0.82) and SCF (0.988) values from the orientation diagnostic job (Figure S2). Both local resolution estimation and global FSC values distinctly indicate resolution range between 3.2 to 3.8 Å.

2. Mnx Forms a Pear-shaped Fold with a Central Tunnel Running Through Both MnxE₃F₃ and MnxG. Our previous Mnx model, ²⁸ obtained with the ab initio prediction tool QUARK, proved to be insufficiently accurate at the atomic level for docking and refinement into the cryo-EM density. Instead, we used the recently available AlphaFold - Multimer algorithm^{29,30} to generate an initial model. Based on the known stoichiometry of the Mnx complex from previous native MS data, ²⁸ 1 copy of MnxG H340A, 3 copies of MnxE, and 3 copies of MnxF sequences were used as input. AlphaFold Multimer code predicted a well-assembled complex, whose structure displayed very high confidence scores except in the N-terminal regions of MnxE and MnxF and for residues involved in protein-protein interactions between MnxG and the MnxE₃F₃ hexamer (Figure S3). This initial computed structure was then successfully docked and subsequently refined into the cryo-EM density, resulting in a tightening of the MnxG-MnxE₃F₃ interface. The low-confidence N-terminal regions of MnxE and MnxF had no cryo-EM density (first 18 amino acids for each), indicating inherent flexibility. Additionally, no distinct density was observed for the C-terminal 10 amino acids for MnxG. These amino acids were excluded in the final model presented in this study. Several representative close-up images depict the cryoEM volume overlaid with the refined atomic structure (Figure S4 and Figure S9). The complex is pear-shaped with MnxE₃F₃ forming the neck (Figure 1). The protein core consists primarily of β-sheets and very long loops. Furthermore, the complex has no symmetry as a whole and, despite its tight fold, the secondary structure content is low especially in its

largest chain, MnxG, similar to other MCO enzymes. The percentages of secondary structure are 28%, 33%, and 42% for MnxG, MnxE, and MnxF, respectively.

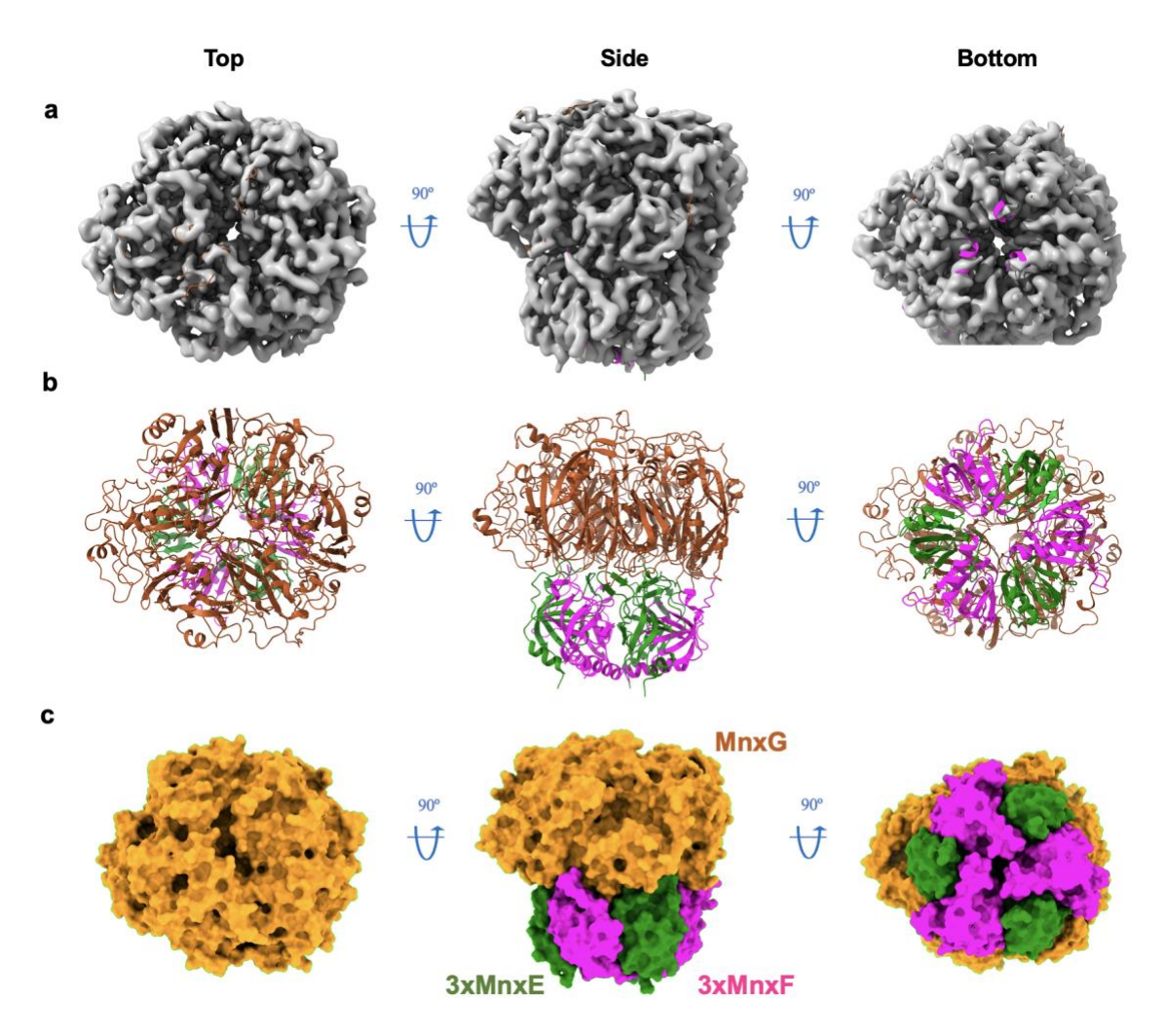


Figure 1. The structure of Mnx H340A. (a) The atomic model of Mnx H340A complex fitted in the unsharpened cryo-EM map (grey mesh). The views are aligned to the central tunnel. The whole complex is asymmetric and was processed in C1 symmetry. (b) The atomic model of Mnx H340A complex. (c) Surface model to highlight topological differences among the subunits.

Critically, the structure showed that the central pore of the MnxE₃F₃ hexamer is directly aligned with a tunnel running through MnxG (Figure 1, top and bottom views). The overall dimensions of the refined structure, 8.7x7.1 nm (Table S2), are consistent with DLS data for this complex showing a mean 8.7 nm hydrodynamic diameter (Figure S5). The measured cross-tunnel distances along its path are in the 0.9–1.1 nm range (Table S2).

To further validate the structural findings, we performed chemical crosslinking and identified 8 intra-protein crosslinks in the MnxG subunit, and 13 inter-protein crosslinks (Figure S6 and S7). Most of them are in reasonable distance agreement with the structure (26–30 Å for alpha carbon distance for the BS3 crosslinker⁴¹). However, select crosslinks fall outside these distance restraints but they are located in loop regions where flexibility is expected. About half of the crosslinks involved terminal regions, including those of MnxE and MnxF, which are unresolved in the structure and imply conformational flexibility at the termini. Wild type Mnx with additional crosslinks gave similar results, fitting within the distance restraints of the H340A structure, indicating structural similarity between the mutant and wild-type. Our previous surface-labeling data²⁸ allocate all labelled residues on the exterior of the complex and not in the MnxG-MnxE₃F₃ binding interface, consistent with the refined protein fold (Figure S8).

3. The Protein Fold and the Catalytic Cu Metal Centers, Mapped by Alignment with Human Ceruloplasmin. MnxG shows a typical MCO-like structural organization, consisting of six cupredoxin-type domains with a Greek-key beta barrel fold, ^{20,42} arranged in a triangular array (Figure 2a) forming a central tunnel. Similar features are found in other MCOs, including human ceruloplasmin (hCp), one of the MnxG's closest homologs. However, compared to hCp, the MnxG domains are arranged in an "inverted order" (Figure 2a). Kosman et. al. first noted these alternative domain orders in MCOs, and suggested an evolutionary origin. ⁴³

Like all MCOs, MnxG uses four copper ions to catalyze substrate oxidation with concomitant oxygen reduction. In our previous EPR study,⁴⁴ 4 additional copper ions, of uncertain function (1 on MnxG and 3 on MnxE₃F₃), were detected.

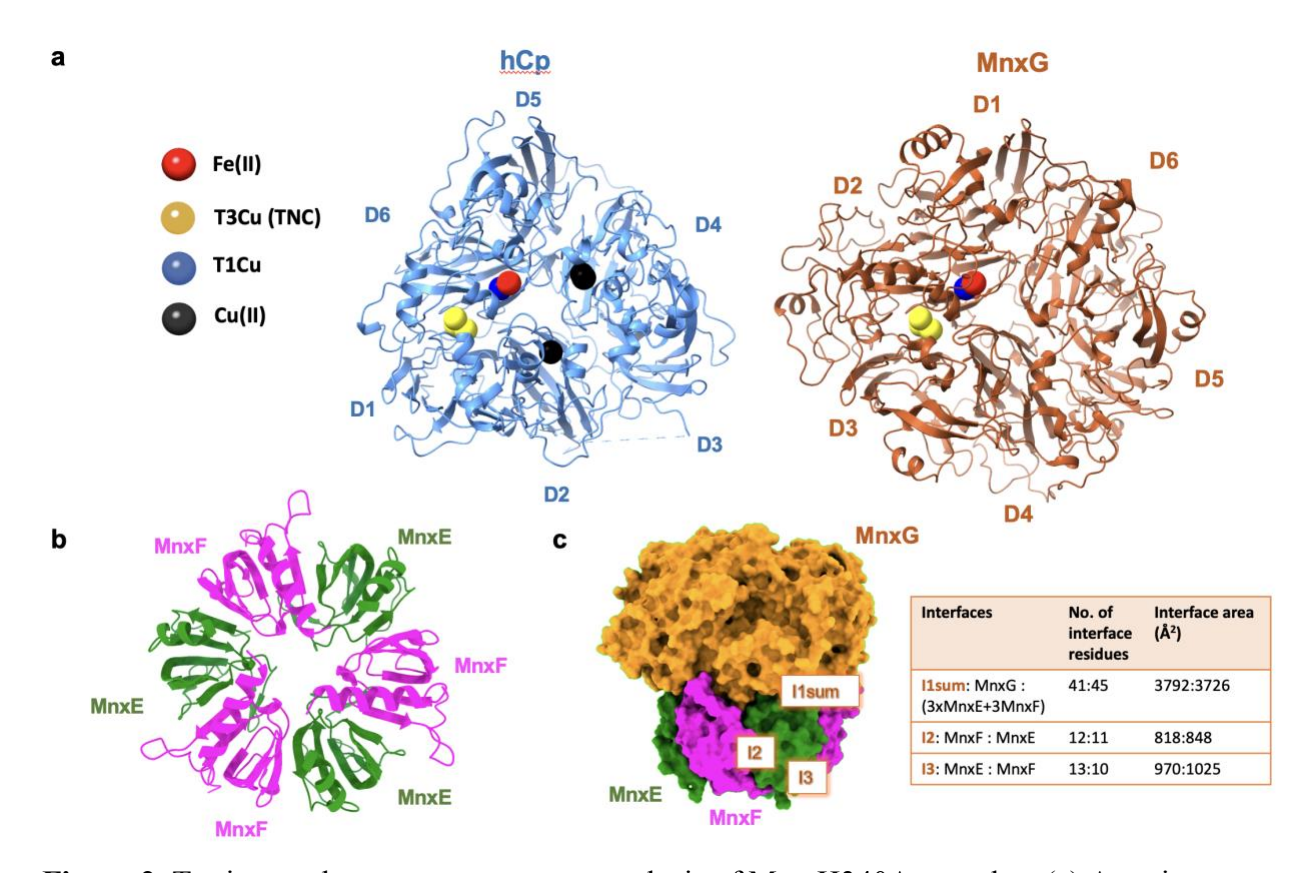


Figure 2. Tertiary and quaternary structure analysis of Mnx H340A complex. (a) Atomic structure comparison between MnxG and a human ceruloplasmin (hCp; PDB ID: 1KCW). Due to a domain inversion, MnxG and hCp structures were aligned on well-conserved regions surrounding the copper binding motifs (as shown in Figure S9a) and then placed side-by-side for easy comparison. The cupredoxin-type domains are annotated as D1 to D6 depending on their order in the sequence. Metal ions from the hCp structure are shown as colored spheres. (b) Atomic structure of MnxE₃F₃ hexamer only. Figures S4 and S9 depict overlaid on the atomic structures cryoEM densities. (c) Analysis of interface binding properties of the complex by PDBsum showed 3 unique interfaces: I1sum, I2 and I3. I1sum data provides the sum of all 6 interfaces between MnxG and its 6 partner MnxE and MnxF proteins. I2 and I3 values provide means for three similar MnxF:MnxE interfaces and MnxE:MnxF interfaces due to heterohexamer formation.

The cryo-EM resolution is insufficient to locate metal ions unambiguously, so we relied on the hCp crystal structure⁴⁵ to predict copper coordination sites by aligning the two structures via the domains containing the catalytically relevant copper centers (domains D1 and D6 in Cp and D2 and D3 in MnxG) (Figure S9). These sites are highly conserved among MCOs. The Mnx structure overlays satisfactorily with that of ceruloplasmin, indicating the usual active site geometry with the type 1 copper site (T1Cu), which extracts an electron from the substrate,

located some 13 Å from the trinuclear copper cluster where O₂ binds. The T1Cu center resides in domain D2 in MnxG (Figure 2a and Figure S9) and is coordinated by three equatorial ligands: one cysteine (C335) and two histidines (H281 and H340), as well as a weak axial ligand, a methionine residue (M345), similar to hCp. Density not occupied by Mnx protein residues clearly links C335 and H281 in the final cryo-EM map, and the overlaid T1Cu atom location from the superimposed hCp structure fits this density well. Also, similar to hCp and other ferroxidases, ^{46,47} the active T1Cu site in MnxG is acidic (Figure 2a and Figure S9), most likely contributing to its low potential measured previously (E₀=0.38 V (pH 7.8)). ²⁶

In MnxG H340A mutant, one of the T1Cu histidine ligands is replaced by a non-coordinating alanine residue. This mutation abolished enzyme activity (Figure S10b), and also the characteristic T1Cu 590 nm absorption band (Figure S10a) and EPR signal,³¹ confirming H340 as a T1-Cu ligand. The MnxG H340A mutant can still bind copper at the T1-Cu site, which could remain spectroscopically silent due to its perturbed electronic structure properties.³¹ However, the H340A replacement has no effect on the CD spectrum (Figure S10c), indicating unchanged secondary structure. Native MS spectra of the H340A are also nearly identical to the wild type Mnx, suggesting unchanged quaternary structure as well (Figure S11).

From the T1-Cu center, the extracted electron is shuttled via the conserved Cys-His superexchange pathway to the trinuclear copper cluster (TNC)—the site of oxygen reduction—which is located at the interface of domains D2 and D3 and ligated by histidine residues (H284, H529, H286, H334, H336, H531, H575, and H577), assigned based on the overlay structure with hCp. Based on the fitted model, density not occupied by protein residues clearly links H336, H531, and H575 as well as H286, H334, and H577 and are the likely locations for 2 of the 3 TNC Cu atoms based on the superposition with hCp (Figure S9).

MnxG binds accessory proteins, a feature unprecedented in other MCOs. MnxE and MnxF form a hexameric MnxE₃F₃ cap, a stable assembly with 3-fold symmetry (Figure 1 and 2b). The MnxG–MnxE₃F₃ interaction (I1sum) is very tight, with an interface area of 3792 Å².

DISCUSSION

While MCO enzymes are efficient one-electron oxidants, manganese-oxidizing MCO MnxG faces the challenge of extracting two successive electrons from high-potential substrates, Mn(II) and Mn(III), en route to the stable MnO₂ product. Moreover, the enzyme must protect itself

against damage from potential highly reactive intermediates. Extensive kinetic and spectroscopic studies have established that MnxG meets these challenges by elegantly exploiting the polynuclear chemistry of manganese. ^{26,27,48} Successive formation of hydroxo-bridged binuclear complexes of Mn(II), Mn(III), and Mn(IV) provides the mechanism of catalysis: kinetic barriers are lowered through the stabilization of high-valent Mn ions by the hydroxide bridges.

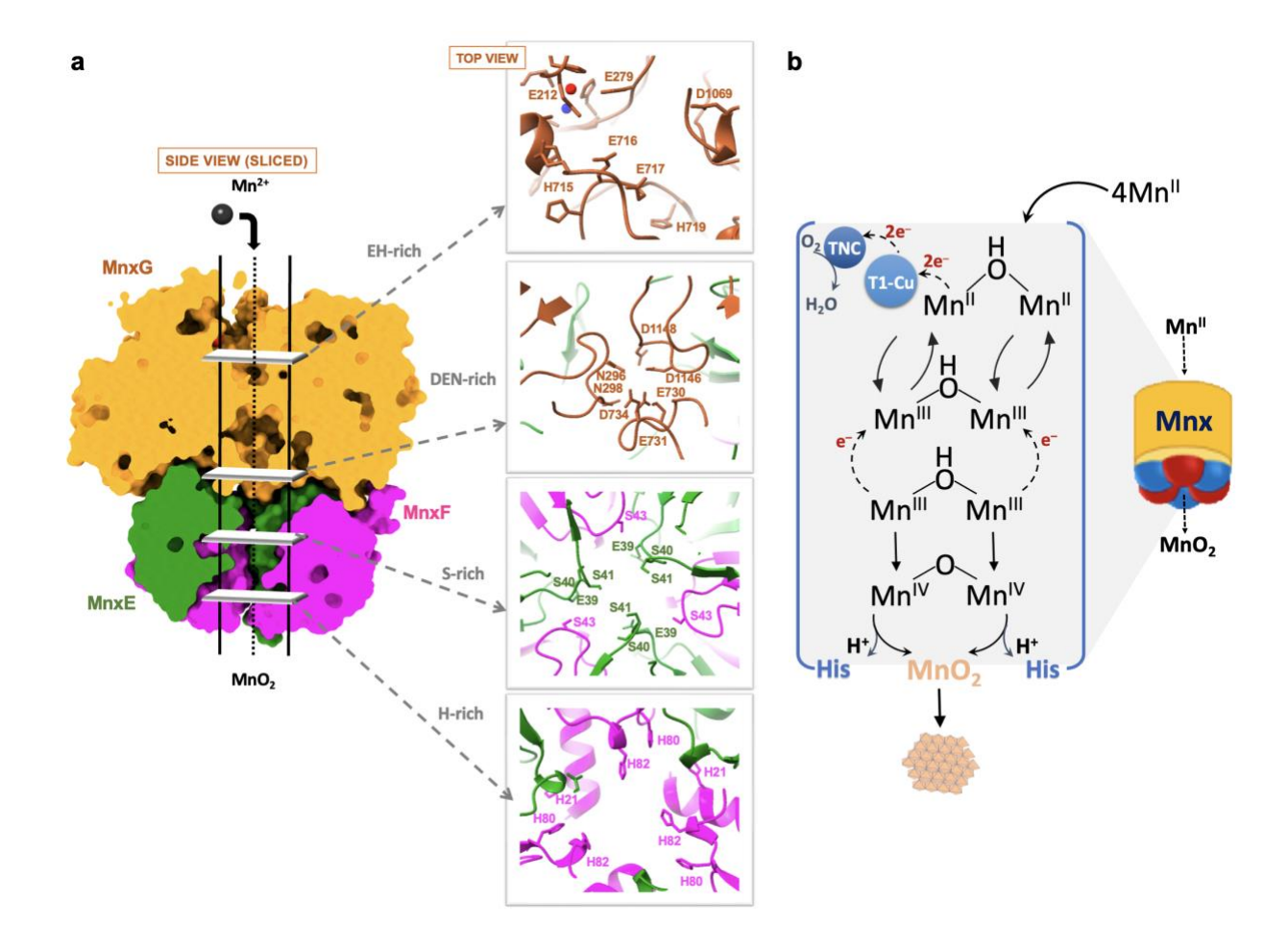


Figure 3. (a) A surface model of Mnx (sliced through the center of the tunnel) and overlaid with its atomic structure, showing the shape and alignment of the MnxG (yellow), MnxE (green) and MnxF (pink) subunits. Black lines on the sliced side view outline the tunnel. The MnxG tunnel is perfectly aligned with the MnxE₃F₃ pore. The black dotted arrow shows the proposed direction of Mn transit. Inner areas of the Mnx tunnel, enriched in charged or polar residues are shown in the insets. (b) Proposed tunnel siting for the Mnx mechanism.

MnxG is unique among MCOs in having accessory proteins, MnxE and MnxF, of unknown function. The present 3D structure reveals how the previously proposed Mnx mechanism could

be facilitated by its most striking feature—the tunnel running straight through MnxG and its MnxE₃F₃ cap (Figure 3). The width of the tunnel (Table S2) can accommodate the binuclear intermediates, while the tunnel-lining residues can stabilize the developing charges of the Mn intermediates.

Similar to other metallooxidases, the Mn(II) substrate likely binds near the T1Cu center, to which it transfers an electron. The T1Cu is close to the entrance of the MnxG tunnel located at the top of the complex. In human ceruloplasmin, ⁴⁵ the Fe(II) substrate (Figure 2a and Figure S9e) is bound to a histidine (H940), a pair of glutamate residues (E935 and E272) and an aspartate residue (D1025), the later having two alternative configurations, pointing outward in the absence of metal. This is similar to the environment around Mn(II) in Mnx based on prior EPR data, ³¹ which showed Mn(II) bound via three caboxylate ligands and one nitrogenous ligand. Our cryo-EM map did not have density associated with the location for Mn(II) which was anticipated, since Mn(II) was absent in the sample buffer and purification steps. However, the superposition with hCp identified density for 3 of the catalytically relevant 4 Cu sites (Figure S9c,d), including the T1-Cu center, lending support to the overall MCO mechanism and suggests that the Mn(II)-binding nitrogenous ligand in Mnx can be identified as H215, which is homologous to the Fe(II)-binding H940 residue of hCp.

In other respects, the coordination environment at the Cp substrate site is altered in MnxG, reflecting the requirement of a second Mn(II) to form the first intermediate, Mn(II)(OH)Mn(II). The D1025 ligand in Cp is replaced by the non-coordinating P339 in MnxG, while hCp's Fe(II) ligand E935 is homologous to E212 in MnxG, though its sidechain is rotated away and points toward an additional potential ligand, E656 (circled in Figure 4). The E212, E656 pair, together with another nearby carboxylate, E716, could form the binding site for the second Mn(II).

The second step in the Mnx mechanism is a cooperative two-electron transfer, forming the Mn(III)(OH)Mn(III) intermediate, which then could be translocated within the tunnel. (This complex may contain additional bridging or terminal OH ligands.) The negatively charged DErich area further down the tunnel (Figure 3) provides stabilization for this more positively charged intermediate. The proposed translocation of Mn(III) during photoassembly of the oxygen-evolving center in photosystem II offers a precedent for movement of high-valent manganese species within the protein interior.⁴⁹ In human Cp, Fe(III) product also migrates

within the protein for the uptake by transferrin or lactoferrin, whose interaction with Cp has been mapped using peptide libraries and modeling studies.⁵⁰ There, the Fe(III)-translocation path leads to the surface of the catalytic domain 6, where lactoferrin transiently binds, bypassing the need for Fe(III) to travel within the Cp's similar tunnel feature. In Cp, the catalytic reaction stops at Fe(III), whereas in Mnx, Mn(III) is an intermediate product, and needs to be stabilized and translocated within the protein for another turnover step to form Mn(IV).

This step, the third one of the Mnx mechanism, requires that two Mn(III)(OH)Mn(III) intermediates interact and disproportionate, to form the next intermediate, Mn(IV)(O)Mn(IV) (again, with additional possible O and OH ligands). Two Mn(II) ions are released in this disproportionation and return to the substrate site to continue the oxidation reaction. The Asp and Glu-rich lower reaches of the tunnel have space enough for this disproportionation step, and the anion-rich walls complement the higher positive charge on Mn(IV)(O)Mn(IV).

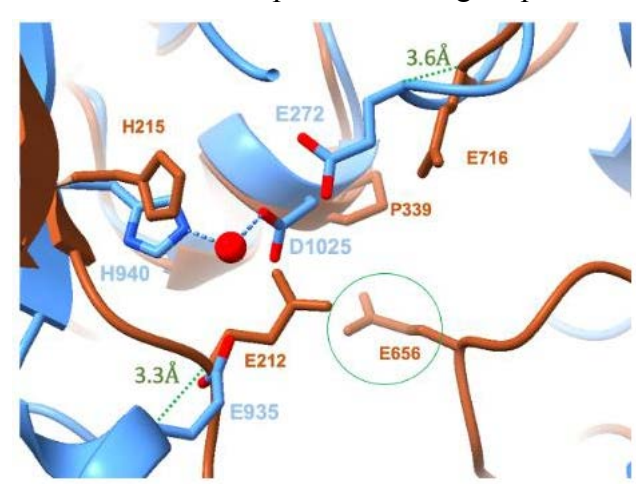


Figure 4. Metal-substrate regions of superimposed MnxG (brown) and hCp (blue) structures, aligned via the T1Cu domains. The red sphere is a Fe(II) ion in the hCp structure (PDB ID: 1KCW).

The Mn(IV)(O)Mn(IV) complex is at the final oxidation level of the MnO₂ product, but it needs to lose protons and condense into nanoparticles. We speculate that this happens as the Mn(IV)(O)Mn(IV) complex migrates further into the perfectly aligned MnxE₃F₃ pore. The pore is lined first with Ser and then with His residues, including a metal-binding motif, H82xxE85, that points into the tunnel. The Ser -OH groups and the His imidazole groups would facilitate deprotonation during successive condensation steps. Two Mn(IV)(O)Mn(IV) complexes likely condense to a Mn(IV)₄O₄ tetramer, whose dimensions could be accommodated near the bottom of the tunnel. A precedent for this protein-mediated condensation is provided by the iron-storage

protein ferritin. In this case, the oxidation product is Fe(III), which travels a 20 Å path lined with histidine, methionine, threonine, glutamate, and serine residues, and condenses inside the protein cavity into hydrous ferric oxide for storage.⁵¹

In Mnx, unlike ferritin, the enzymatically produced MnO₂ is not confined within the protein and must be expelled, to allow subsequent turnovers. Histidine residues at the MnxE₃F₃ pore exit can potentially support further condensation of the MnO₂ product via the required deprotonation, allowing release of the nanoparticles⁵² (Figure 3). The N-terminal regions, presumed to be flexible due to the lack of cryo-EM density, may assist in the departure of the growing mineral product. The proposed direction of the flow of substrate and departing product is further supported by Mnx surface charge distribution calculations in Figure S12, showing a distinct negative region at the top of the MnxG complex around the central tunnel, which could assist in attracting the positively charged Mn(II) substrate close to the binding site next to the T1Cu center. The opposite side of the Mnx complex, MnxE₃F₃, is mostly neutral, which could facilitate departure of the MnO₂ product, whose net charge is expected to be negative at neutral pH.

CONCLUSION

Being an important biological and technological class of metalloenzymes, multicopper oxidases are extensively investigated. However, manganese-oxidizing bacterial MCO MnxG, with its novel bioinorganic chemistry of manganese oxidation and biomineral formation, represents an entirely new subclass. Up until now, the structural details of its complex assembly remained hidden. Breakthroughs in biochemical techniques, and advances in cryo-EM microscopy and in protein structure prediction unveiled atomic level details of the only purified manganese-oxidizing MCO protein Mnx, reported here. The identified Mnx tunnel and MnxE₃F₃ pore are the most striking features of the Mnx complex and provide an attractive hypothesis for a well-evolved pathway for the unique chemical mechanism of Mn(II) oxidation, together with the required condensation and deprotonation of the initial oxidation products to produce nanoparticulate MnO₂ biomineral. The structure offers a platform for further experiments to elucidate mechanistic details of manganese biomineralization.

ASSOCIATED CONTENT

Supporting Information

The Supporting Information is available free of charge on the ACS Publications website.

Cryo-EM single particle analysis workflow and tabulated metadata; data quality diagnostic analysis, the reconstructed map, electrostatic potential, and hydrophobic maps of Mnx protein mutant; initial AlphaFold2-multimer model refined into the cryo-EM map; structure-based alignment of Mnx mutant with human ceruloplasmin; tabulated distance measurements of the main features of Mnx structure; Mnx protein and its mutant characterization by dynamic light scattering, UV-vis absorption spectroscopy, kinetic measurements, and crosslinking and native MS/

Data availability

The final model of Mnx H340A protein and its cryo-EM map have been uploaded to the PDB and EMDB databases under the accession numbers PDB 9BXA and EMD-45001. The raw cryoEM micrographs have been deposited in the EMPIAR database and assigned the accession number EMPIAR-12107. All mass spectrometry data and processed crosslinking files are available at

https://massive.ucsd.edu/ProteoSAFe/dataset.jsp?task=1c85303a4cbd406c896544c7e358a6bf.

AUTHOR INFORMATION

Corresponding Author

*T.G.S.: spirot@uw.edu and J. E. E.: james.evans@pnnl.gov

Present Addresses

¤Stylus Medicine, Inc, 200 Berkeley Street, Boston, MA 02116, United States

+Department of Chemistry, Zhejiang University, 866 Yuhangtang Road, Hangzhou, Zhejiang 310058, China

Author Contributions

The manuscript was written through contributions of all authors. / All authors have given approval to the final version of the manuscript. /

§I.V.N. and A.V.S. contributed equally to this work.

Notes

The authors declare no competing financial interest.

ACKNOWLEDGMENT

This work was supported by the National Science Foundation: award numbers CHE-1410353, CHE-1807222, and EAR-1951143 to TGS, and CHE-1410688, CHE-1807158, CHE-2120408 and EAR-2122086 to BMT. The cryo-EM and MS work were performed at the Environmental Molecular Science Laboratory (EMSL), a Department of Energy (DOE) Office of Science User Facility sponsored by the Office of Biological and Environmental Research, under project 50773 (https://doi.org/10.46936/lser.proj.2019.50773/60000097). The modification parts for the surface induced dissociation device for the native MS experiments were kindly provided by the Wysocki group at Ohio State University under funding by the NIH National Institute of General Sciences (P41GM128577). Molecular graphics and analyses per-formed with UCSF Chimera or ChimeraX, developed by the Resource for Biocomputing, Visualization, and Informatics at the University of California, San Francisco, with support from National Institutes of Health R01-GM129325 and the Office of Cyber Infrastructure and Computational Biology, National Institute of Allergy and Infectious Diseases.

REFERENCES

- (1) Morgan, J. J. Manganese in Natural Waters and Earth's Crust: Its availability to organisms. In *Metal Ions in Biological Systems: Manganese and Its Role in Biological Processes*; Sigel, A., Sigel, H., Eds.; Marcel Dekker: New York, 2000; pp 1–34.
- (2) Myers, C. R.; Nealson, K. H. Bacterial manganese reduction and growth with manganese oxide as the sole electron-acceptor. *Science* **1988**, *240*, 1319–1321.
- (3) Lovley, D. R. Dissimilatory Fe(III) and Mn(IV) reduction. *Microbiol. Rev.* **1991**, *55*, 259–287.
- (4) Lin, H.; Szeinbaum, N. H.; DiChristina, T. J.; Taillefert, M. Microbial Mn(IV) reduction requires an initial one-electron reductive solubilization step. *Geochim. Cosmochim. Acta* **2012**, *99*, 179–192.
- (5) Tebo, B. M; Bargar, J. R.; Clement, B.; Dick, G.; Murray, K. J.; Parker, D.; Verity, R.; Webb, S. M. Biogenic manganese oxides: Properties and mechanisms of formation. *Annu. Rev. Earth Planet. Sci.* **2004**, *32*, 287–328.

- (6) Miyata, N.; Tani, Y.; Sakata, M.; Iwahori, K. Microbial manganese oxide formation and interaction with toxic metal ions. *J. Biosci. Bioengin.* **2007**, *104*, 1–8.
- (7) Hansel, C. M.; Ferdelman, T. G.; Tebo, B. M. Cryptic cross-linkages among biogeochemical cycles: Novel insights from reactive intermediates. *Elements* **2015**, *11*, 409–414.
- (8) Tebo, B. M.; Johnson, H. A.; McCarthy, J. K.; Templeton, A. S. Geomicrobiology of manganese(II) oxidation. *Trends Microbiol.* **2005**, *13*, 421–428.
- (9) Santelli, C. M.; Webb, S. M.; Dohnalkova, A. C.; Hansel, C. M. Diversity of Mn oxides produced by Mn(II)-oxidizing fungi. *Geochim. Cosmochim. Acta* **2011**, *75*, 2762–2776.
- (10) Sunda, W. G.; Kieber, D. J. Oxidation of humic substances by manganese oxides yields low-molecular-weight organic substrates. *Nature* **1994**, *367*, 62–64.
- (11) Spiro, T. G.; Bargar, J. R.; Sposito, G.; Tebo, B. M. Bacteriogenic manganese oxides. *Acc. Chem. Res.* **2010**, *43*, 2–9.
- (12) Yu, H.; Leadbetter, J. R. Bacterial chemolithoautotrophy via manganese oxidation. *Nature* **2020**, *583*, 453–458.
- (13) van Waasbergen, L. G.; Hildebrand, M.; Tebo, B. M. Identification and characterization of a gene cluster involved in manganese oxidation by spores of the marine *Bacillus* sp. strain SG-1. *J. Bacteriology* **1996**, *178*, 3517–3530.
- (14) Corstjens, P. L. A. M.; de Vrind, J. P. M.; Goosen, T.; de Vrind-de Jong, E. W. Identification and molecular analysis of the *Leptothrix discophora* SS-1 mofA gene a gene putatively encoding a manganese-oxidizing protein with copper domains. *Geomicrobiol. J.* **1997**, *14*, 91–108.
- (15) Okazaki, M.; Sugita, T.; Shimizu, M.; Ohode, Y.; Iwamoto, K.; de Vrind-de Jong, E. W.; de Vrind, J. P. M.; Corstjens, P. L. A. M. Partial purification and characterization of manganese-oxidizing factors of *Pseudomonas fluorescens* GB-1. *Appl. Environ. Microbiol.* **1997**, *63*, 4793–4799.
- (16) Larsen, E. I.; Sly, L. I.; McEwan, A. G. Manganese(II) adsorption and oxidation by whole cells and a membrane fraction of *Pedomicrobium* sp. ACM 3067. *Arch. Microbiol.* **1999**, *171*, 257–264.
- (17) Brouwers, G. J.; Corstjens, P. L. A. M.; de Vrind, J. P. M.; Verkamman, A.; de Kuyper, M.; de Vrind-de Jong, E. W. Stimulation of Mn²⁺ oxidation in *Leptothrix discophora* SS-1 by Cu²⁺

- and sequence analysis of the region flanking the gene encoding putative multicopper oxidase MofA. *Geomicrobiol. J.* **2000**, *17*, 25–33.
- (18) Ridge, J. P.; Lin, M.; Larsen, E. I.; Fegan, M.; McEwan, A. G.; Sly, L. I. A multicopper oxidase is essential for manganese oxidation and laccase-like activity in *Pedomicrobium* sp. ACM 3067. *Environ. Microbiol.* **2007**, *9*, 944–953.
- (19) Geszvain, K.; Butterfield, C. N.; Davis, R. E.; Madi-son, A. S.; Lee, S.-W.; Parker, D. L.; Soldatova, A. V.; Spiro, T. G.; Luther III, G. W.; Tebo, B. M. The molecular biogeochemistry of manganese(II) oxidation. *Biochem. Soc. Trans.* **2012**, *40*, 1244–1248.
- (20) Solomon, E. I.; Sundaram, U. M.; Machonkin, T. E. Multicopper oxidases and oxygenases. *Chem. Rev.* **1996**, *96*, 2563–2605.
- (21) Kosman, D. J. Multicopper oxidases: a workshop on copper coordination chemistry, electron transfer, and metallophysiology. *J. Biol. Inorg. Chem.* **2010**, *15*, 15–28.
- (22) Butterfield, C. N.; Soldatova, A. V.; Lee, S.-W.; Spiro, T. G.; Tebo, B. M. Mn(II,III) oxidation and MnO₂ mineralization by an expressed bacterial multicopper oxidase. *Proc. Natl. Acad. Sci. U. S. A.* **2013**, *110*, 11731–11735.
- (23) van Waasbergen, L. G.; Hoch, J. A.; Tebo, B. M. Genetic analysis of the marine manganese-oxidizing *Bacillus* sp. strain SG-1: protoplast transformation, Tn917 mutagenesis, and identification of chromosomal loci involved in manganese oxidation. *J. Bacteriol.* **1993**, *175*, 7594–7603.
- (24) Dick, G. J.; Torpey, J. W.; Beveridge, T. J.; Tebo, B. M. Direct identification of a bacterial manganese(II) oxidase, the multicopper oxidase MnxG, from spores of several different marine *Bacillus* species. *Appl. Environ. Microbiol.* **2008**, *74*, 1527–1534.
- (25) Butterfield, C. N.; Tao, L.; Chacón, K. N.; Spiro, T. G.; Blackburn, N. J.; Casey, W. H.; Britt, R. D.; Tebo, B. M. Multicopper manganese oxidase accessory proteins bind Cu and heme. *Biochim. Biophys. Acta* **2015**, *1854*, 1853–1859.
- (26) Soldatova, A. V.; Tao, L.; Romano, C.; Stich, T. A.; Casey, W. H.; Britt, R. D.; Tebo, B. M.; Spiro, T. G. Mn(II) oxidation by the multicopper oxidase complex Mnx: A binuclear activation mechanism. *J. Am. Chem. Soc.* **2017**, *139*, 11369–11380.
- (27) Soldatova, A. V.; Romano, C.; Tao, L.; Stich, T. A.; Casey, W. H.; Britt, R. D.; Tebo, B. M.; Spiro, T. G. Mn(II) oxidation by the multicopper oxidase complex Mnx: A coordinated two-stage MnII/MnIII and MnIII/MnIV mechanism. *J. Am. Chem. Soc.* **2017**, *139*, 11381–11391.

- (28) Romano, C. A.; Zhou, M.; Song, Y.; Wysocki, V. H.; Dohnalkova, A. C.; Kovarik, L.; Paša-Tolić, L.; Tebo, B. M. Biogenic manganese oxide nanoparticle formation by a multimeric multicopper oxidase Mnx. *Nat. Commun.* **2017**, *8*, 746.
- (29) Jumper, J.; Evans, R.; Pritzel, A.; Green, T.; Figurnov, M.; Ronneberger, O.;
 Tunyasuvunakool, K.; Bates, R.; Žídek, A.; Potapenko, A.; Bridgland, A.; Meyer, C.; Kohl, S. A. A.; Ballard, A. J.; Cowie, A.; Romera-Paredes, B.; Nikolov, S.; Jain, R.; Adler, J.; Back, T.; Petersen, S.; Reiman, D.; Clancy, E.; Zielinski, M.; Steinegger, M.; Pacholska, M.; Berghammer, T.; Bodenstein, S.; Silver, D.; Vinyals, O.; Senior, A. W.; Kavukcuoglu, K.; Kohli, P.; Hassabis, D. Highly accurate protein structure prediction with AlphaFold. *Nature* 2021, *596*, 583–589.

 (30) Evans, R.; O'Neill, M.; Pritzel, A.; Antropova, N.; Senior, A.; Green, T.; Žídek, A.; Bates, R.; Blackwell, S.; Yim, J.; Ronneberger, O.; Bodenstein, S.; Zielinski, M.; Bridgland, A.; Potapenko, A.; Cowie, A.; Tunyasuvunakool, K.; Jain, R.; Clancy, E.; Kohli, P.; Jumper, J.; Hassabis, D. Protein complex prediction with AlphaFold-Multimer. *Preprint at BioRxiv* 2021,
- (31) Tao, L.; Stich, T. A.; Butterfield, C. N.; Romano, C. A.; Spiro, T. G.; Tebo, B. M.; Casey, W. H.; Britt, R. D. Mn(II) binding and subsequent oxidation by the multicopper oxidase MnxG investigated by electron paramagnetic resonance spectroscopy. *J. Am. Chem. Soc.* **2015**, *137*, 10563–10575.

https://doi.org/10.1101/2021.10.04.463034.

- (32) Punjani, A.; Rubinstein, J. L.; Fleet, D. J.; Brubaker, M. A. cryoSPARC: algorithms for rapid unsupervised cryo-EM structure determination. *Nat. Methods* **2017**, *14*, 290–296.
- (33) Rubinstein, J. L.; Brubaker, M. A. Alignment of cryo-EM movies of individual particles by optimization of image translations. *J. Struct. Biol.* **2015**, *192*, 188–195.
- (34) Pettersen, E. F.; Goddard, T. D.; Huang, C. C.; Meng, E. C.; Couch, G. S.; Croll, T. I.; Morris, J. H.; Ferrin, T. E. UCSF ChimeraX: Structure visualization for researchers, educators, and developers. *Protein Sci.* **2021**, *30*, 70–82.
- (35) Goddard, T. D.; Huang, C. C.; Meng, E. C.; Pettersen, E. F.; Couch, G. S.; Morris, J. H.; Ferrin, T. E. UCSF ChimeraX: Meeting modern challenges in visualization and analysis. *Protein Sci.* **2018**, *27*, 14–25.
- (36) Liebschner, D.; Afonine, P. V.; Baker, M. L.; Bunkóczi, G.; Chen, V. B.; Croll, T. I.; Hintze, B.; Hung, L. W.; Jain, S.; McCoy, A. J.; Moriarty, N. W.; Oeffner, R. D.; Poon, B. K.; Prisant, M. G.; Read, R. J.; Richardson, J. S.; Richardson, D. C.; Sammito, M. D.; Sobolev, O.

- V.; Stock-well, D. H.; Terwilliger, T. C.; Urzhumtsev, A. G.; Videau, L. L.; Williams, C. J.; Adams, P. D. Macromolecular structure determination using X-rays, neutrons and electrons: recent developments in Phenix. *Acta Cryst.* **2019**, *D75*, 861–877.
- (37) Adusumilli, R.; Mallick, P. Data Conversion with ProteoWizard msConvert. In *Proteomics*. *Methods in Molecular Biology*; Comai, L., Katz, J., Mallick, P., Eds.; Humana Press: New York, 2017; pp 339–368.
- (38) Götze, M.; Iacobucci, C.; Ihling, C. H.; Sinz, A. A simple cross-linking/mass spectrometry workflow for studying system-wide protein interaction. *Anal. Chem.* **2019**, *91*, 10236–10244.
- (39) Chen, Z.-L.; Meng, J.-M.; Cao, Y.; Yin, J.-L.; Fang, R.-Q.; Fan, S.-B.; Liu, C.; Zeng, W.-F.; Ding, Y.-H.; Tan, D.; Wu, L.; Zhou, W.-J.; Chi, H.; Sun, R.-X.; Dong, M.-Q.; He, S.-M. A high-speed search engine pLink 2 with systematic evaluation for proteome-scale identification of cross-linked peptides. *Nat. Commun.* **2019**, *10*, 3404.
- (40) Snyder, D. T.; Panczyk, E. M.; Somogyi, A.; Kaplan, D. A.; Wysocki, V. Simple and minimally invasive SID devices for native mass spectrometry. *Anal. Chem.* **2020**, *92*, 11195–11203.
- (41) Merkley, E. D.; Rysavy, S.; Kahraman, A.; Hafen, R. P.; Daggett, V.; Adkins, J. N. Distance restraints from cross-linking mass spectrometry: Mining a molecular dynamics simulation database to evaluate lysine–lysine distances. *Protein Sci.* **2014**, *23*, 747–759.
- (42) Colman, P.; Freeman, H. C.; Guss, J. M.; Murata, M.; Norris, V. A.; Ramshaw, J. A. M.; Venkatappa, M. P. X-ray crystal structure analysis of plastocyanin at 2.7 Å resolution. *Nature* **1978**, *272*, 319–324.
- (43) Terzulli, A. J.; Kosman, D. J. The Fox1 ferroxidase of *Chlamydomonas reinhardtii*: a new multicopper oxidase structural paradigm. *J. Biol. Inorg. Chem.* **2009**, *14*, 315–325.
- (44) Tao, L.; Stich, T. A.; Liou, S.-H.; Soldatova, A. V.; Delgadillo, D. A.; Romano, C. A.; Spiro, T. G.; Goodin, D. B.; Tebo, B. M.; Casey, W. H.; Britt, R. D. Copper binding sites in the manganese-oxidizing Mnx protein complex investigated by Electron Paramagnetic Resonance spectroscopy. *J. Am. Chem. Soc.* **2017**, *139*, 8868–8877.
- (45) Lindley, P. F.; Card, G.; Zaitseva, I.; Zaitsev, V.; Reinhammar, B.; Selin-Lindgren, E.; Yoshida, K. An X-ray structural study of human ceruloplasmin in relation to ferroxidase activity. *J. Biol. Inorg. Chem.* **1997**, *2*, 454–463.

- (46) Singha, A.; Sekretareva, A.; Tao, L.; Lim, H.; Ha, Y.; Braun, A.; Jones, S. M.; Hedman, B.; Hodgson, K. O.; Britt, R. D.; Kosman, D. J.; Solomon, E. I. Tuning the type 1 reduction potential of multicopper oxidases: Uncoupling the effects of electrostatics and H-bonding to histidine ligands. *J. Am. Chem. Soc.* **2023**, *145*, 13284–13301.
- (47) Quintanar, L.; Stoj, C.; Taylor, A. B.; Hart, P. J.; Kosman, D. J.; Solomon, E. I. Shall we dance? How a multi-copper oxidase chooses its electron transfer partner. *Acc. Chem. Res.* **2007**, *40*, 445–452.
- (48) Tao, L.; Stich, T. A.; Soldatova, A. V.; Tebo, B. M.; Spiro, T. G.; Casey, W. H.; Britt, R. D. Mn(III) species formed by the multicopper oxidase MnxG investigated by electron paramagnetic resonance spectroscopy. *J. Biol. Inorg. Chem.* **2018**, *23*, 1093–1104.
- (49) Oliver, N.; Avramov, A. P.; Nürnberg, D. J.; Dau, H.; Burnap, R. L. From manganese oxidation to water oxidation: assembly and evolution of the water-splitting complex in photosystem II. *Photosynth. Res.* **2022**, *152*, 107–133.
- (50) White, K. N.; Conesa, C.; Sánchez, L.; Amini, M.; Farnaud, S.; Lorvoralak, C.; Evans, R. W. The transfer of iron between ceruloplasmin and transferrins. *Biochim. Biophys. Acta* **2012**, *1820*, 411–416.
- (51) Turano, P.; Lalli, D.; Felli, I. C.; Theil, E. C.; Bertini, I. NMR reveals pathway for ferric mineral precursors to the central cavity of ferritin. *Proc. Natl. Acad. Sci. U. S. A.* **2010**, *107*, 545–550.
- (52) Soldatova, A. V.; Balakrishnan, G.; Oyerinde, O. F.; Romano, C. A.; Tebo, B. M.; Spiro, T. G. Biogenic and synthetic MnO₂ nanoparticles: Size and growth probed with absorption and Raman spectroscopies and dynamic light scattering. *Environ. Sci. Technol.* **2019**, *53*, 4185–4197.